ADVANCED FUNCTIONAL MATERIALS
www.afm-journal.de

Highly Efficient Inverted Organic Solar Cells Through Material and Interfacial Engineering of Indacenodithieno[3,2-*b*]thiophene-Based Polymers and Devices

Jeremy J. Intemann, Kai Yao, Yong-Xi Li, Hin-Lap Yip, Yun-Xiang Xu, Po-Wei Liang, Chu-Chen Chueh, Fei-Zhi Ding, Xi Yang, Xiaosong Li, Yiwang Chen, and Alex K.-Y. Jen**

A synergistic approach combining new material design and interfacial engineering of devices is adopted to produce high efficiency inverted solar cells. Two new polymers, based on an indacenodithieno[3,2-*b*]thiophene-difluorobenzothiadiazole (PIDTT-DFBT) donor–acceptor (D–A) polymer, are produced by incorporating either an alkyl thiophene (PIDTT-DFBT-T) or alkyl thieno[3,2-b] thiophene (PIDTT-DFBT-TT) π-bridge as spacer. Although the PIDTT-DFBT-TT polymer exhibits decreased absorption at longer wavelengths and increased absorption at higher energy wavelengths, it shows higher power conversion efficiencies in devices. In contrast, the thiophene bridged PIDTT-DFBT-T shows a similar change in its absorption spectrum, but its low molecular weight leads to reduced hole mobilities and performance in photovoltaic cells. Inverted solar cells based on PIDTT-DFBT-TT are explored by modifying the electron-transporting ZnO layer with a fullerene self-assembled monolayer and the MoO_3 hole-transporting layer with graphene oxide. This leads to power conversion efficiencies as high as 7.3% in inverted cells. PIDTT-DFBT-TT's characteristic strong short wavelength absorption and high efficiency suggests it is a good candidate as a wide band gap material for tandem solar cells.

1. Introduction

The field of organic photovoltaics (OPVs) has seen rapid progress over the past few years due to concerted efforts in developing semiconducting polymers with properly balanced energy levels, band gap, charge carrier mobilities, and film-forming properties.[1] In addition, parallel advances in device engineering have also led to rapid improvement, such as incorporating interfacial layers to improve charge transport and collection,[2] controlling morphology through solvent additives,[3] improving device stability through inverted architectures,[4] and enhancing light harvesting using tandem cells.[5] These collective efforts have produced OPVs with power conversion efficiencies (PCE) well over 9% in single-junction devices[6] and as high as 10.6% in tandem cells.[7]

Among different device architectures used so far, the conventional bulk-heterojunction (BHJ) cells often encounter stability issues due to the permeation of moisture and oxygen into devices. Oxygen tends to create trap states in the active layer, reducing exciton dissociation efficiency,[8] while oxidation of the low work-function cathode and water adsorption by the hygroscopic PEDOT:PSS hole-transporting layer reduces mobilities and increases charge injection barriers.[9] To circumvent these problems, an inverted device structure with air-stable high-work-function metals (such as Ag and Au) are used as the anode with a high work function air-stable transition metal oxide, such as VO_x,[10] NiO_x,[11] or MoO_3,[12] while the ITO electrode is modified with a stable low-work-function metal oxide buffer layer, such as ZnO[13] or TiO_x.[14] Through this device architecture change, environmental stability is improved because the air-stable high work function metal electrode serves to self-encapsulate the device and an ITO/PEDOT:PSS interface is avoided.[15] Despite significant improvement in the environmental stability, inverted solar cells still suffer from a trade-off between stability and performance.[16] The deteriorated electrical properties at the interface between metal oxide and organic layers are caused by unfavorable energetics, incompatible chemical interfaces, and the formation of electron trap states on the surface of the metal oxide, which is detrimental to performance.[17] Therefore, the development of efficient inverted OPVs not only requires developing diverse OPV architectures with appropriate BHJ active

Dr. J. J. Intemann, K. Yao, Y.-X. Li, Dr. H.-L. Yip, Dr. Y.-X. Xu, P.-W. Liang, Dr. C.-C. Chueh, X. Yang, Prof. A. K.-Y. Jen
Department of Materials Science and Engineering
University of Washington
Seattle, WA, 98195–2120, United States
E-mail: ajen@u.washington.edu
K. Yao, Prof. Y. Chen
Institute of Polymers/Department of Chemistry
Nanchang University
999 Xuefu Avenue, Nanchang, 330031, China
E-mail: ywchen@ncu.edu.cn
F.-Z. Ding, Prof. X. Li
Department of Chemistry
University of Washington
Seattle, WA, 98195–1700, USA

DOI: 10.1002/adfm.201302426

© 2013 WILEY-VCH Verlag GmbH & Co. KGaA, Weinheim

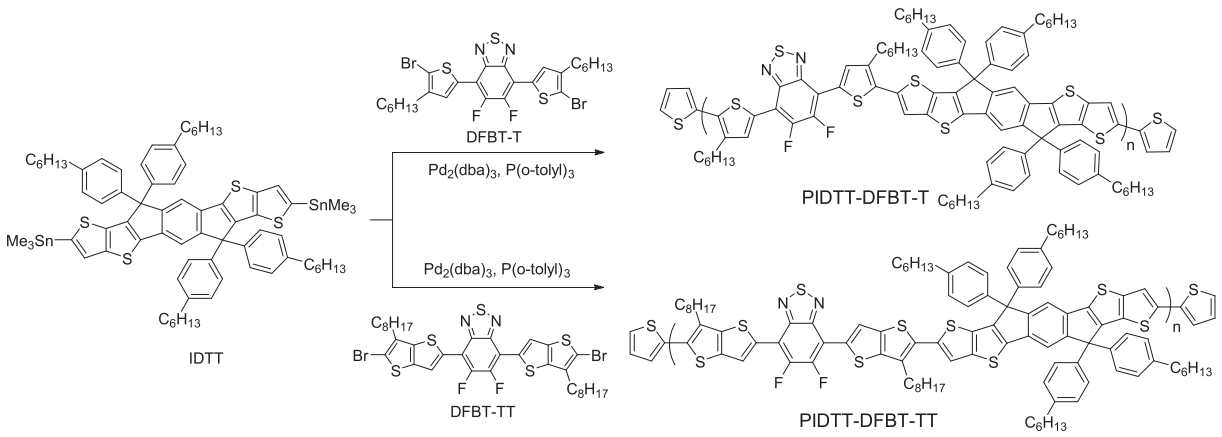

Scheme 1. Synthesis of PIDTT-DFBT-T and PIDTT-DFBT-TT.

materials, but also understanding how to manipulate charge selectivity through interfacial modifications. For the electron transporting layers (ETLs), taking ZnO as an example, several representative interfacial modification materials have been examined, such as a self-assembled monolayer (SAM) derived from C_{60}-substituted benzoic acid (C_{60}-COOH),[18] poly[(9,9-bis(3′-(N,N-dimethylamino)propyl)-2,7-fluorene)-alt-2,7-(9,9-dioctylfluorene)] (PFN-Br),[6c] and 80% ethoxylated polyethylenimine (PEIE).[19] These materials have been used to improve performance through tuning of the ZnO work function, decreasing the contact resistance, and reducing surface electron traps, which results in an improvement in performance to over 8%. As for the hole transporting layers (HTLs), thermally evaporated metal oxides, such as evaporated MoO_3, have provided high efficiencies in inverted OPVs, with a remarkable PCE of 9.2% achieved in a PTB7:PC_{71}BM system.[6a] However, the PCEs observed from many inverted devices are still not comparable to those obtained from the conventional device configuration, and the development of new HTLs for inverted PSCs remains open.

From a material perspective, it is desirable for the donor polymer to be insensitive to processing conditions, while having a good morphology that can lead to high efficiency devices. This not only reduces the complexity of device fabrication but also provides better reproducibility in device performance. However, many high-performance semiconducting polymers reported in the literature require extensive manipulation of the morphology through solvent additives and meticulous annealing procedures.[20] Recently, we have reported a new ladder-type D–A alternating copolymer poly[(indacenodithieno[3,2-*b*]thiophene)-alt-difluorobenzothiadiazole] (PIDTT-DFBT), which gave power conversion efficiencies in devices of 7% without using any solvent additives or post processing techniques.[21] PIDTT-DFBT possesses a low-lying HOMO, giving devices made from it a high V_{OC} of nearly 1 V, while its high extinction coefficient and hole mobility result in a photocurrent of 12.2 mA cm^{-2}. This led us to explore further structural optimization of PIDTT-DFBT to attempt to enhance its performance.

Incorporation of a π-bridge, such as thiophene or thieno[3,2-*b*]thiophene (TT), between the donor and acceptor moieties in semiconducting polymers tends to enhance the effective conjugation length and hole mobilities of the corresponding polymers,[20a,22] resulting in enhanced OPV performance. TT, in particular, has advantages over thiophene as a π-bridge, as it's more linear structure gives its polymers a more persistent rod-like structure, improving the polymer's ability to π-stack efficiently. We have previously reported the incorporation of thiophene, TT, and 6-octylthieno[3,2-*b*]thiophene (OTT) as a π-bridge in a Pt-based donor polymer.[23]

It was found that the use of OTT provided the highest charge carrier mobilities and device efficiencies. These results, coupled with the limited solubility of PIDTT-DFBT, suggests that incorporating alkyl thiophene and alkyl thieno[3,2-b]thiophene into PIDTT-DFBT as π-bridges would improve the properties, solubility, and performance of PIDTT-DFBT. Herein, we report two new polymers based on PIDTT-DFBT, integrating 3-hexylthiophene and 3-octylthieno[3,2-b]thiophene as π-bridges, namely, poly[indacenodithieno[3,2-b]thiophene-alt-(4,7-bis(4-hexylthiophen-2-yl)-5,6-difluoro-[3,1,2]benzothiadiazole)] (PIDTT-DFBT-T) and poly[indacenodithieno[3,2-*b*] thiophene-alt-(4,7-bis(6-octylthieno[3,2-b]thiophen-2-yl)-5,6-difluoro-[3,1,2] benzothiadiazole)] (PIDTT-DFBT-TT) (**Scheme 1**). The photovoltaic performance of the polymers is investigated in conventional cells and the optimization of PIDTT-DFBT-TT in inverted cells is explored through interfacial layer modification of devices. By casting a self-assembled monolayer onto ZnO film and thin graphene oxide onto the BHJ film, the interface between ZnO electron extraction layer and the active layer, as well as the interface between BHJ film and the MoO_3 hole transporting layer are re-engineered, respectively.

2. Results and Discussion

2.1. Polymer Synthesis and Characterization

The polymers PIDTT-DFBT-T and PIDTT-DFBT-TT were prepared via Stille polymerization of the monomer IDTT and either DFBT-T or DFBT-TT using a $Pd_2(dba)_3$ catalyst and P(o-tolyl)$_3$ ligand in refluxing toluene. Before quenching the polymerization reactions, 2-tributylstannylthiophene and 2-bromothiophene were added sequentially to end cap the polymer

© 2013 WILEY-VCH Verlag GmbH & Co. KGaA, Weinheim

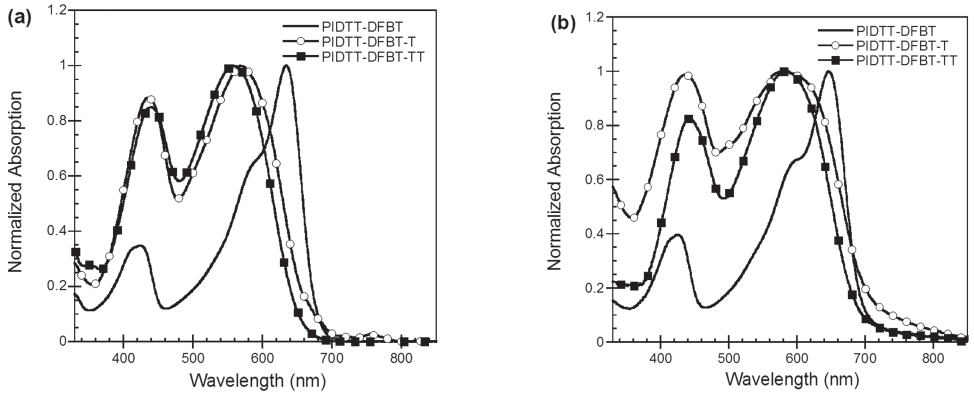

Figure 1. UV spectra of polymers in a) solutions of chlorobenzene and as b) thin films.

chains with thiophene. This prevents reactive end groups from acting as charge trapping sites in electronic devices.[24] The polymers were purified by precipitation in methanol followed by Soxhlet extraction with acetone and hexane to remove residual catalyst and low molecular weight oligomers. The polymers were then dissolved in chloroform and precipitated again into methanol.

PIDTT-DFBT-T possessed a rather low molecular weight of 11.3 kDa with a PDI of 1.9 and had poor solubility in solvents other than chlorobenzene and o-dichlorobenzne (*o*-DCB). PIDTT-DFBT-TT, on the other hand, had a moderate molecular weight of 19.7 kDa and a PDI of 2.3, while possessing good solubility in chloroform, THF, and *o*-DCB, possibly due to its slightly longer alkyl chain. Differential scanning calorimetry of PIDTT-DFBT-T and PIDTT-DFBT-TT showed no thermal transitions between 20 and 200 °C (see Figure S1 of the Supporting Information), common to IDTT-based polymers as the 4-hexylphenyl side chains are known to prevent ordered packing, making the polymer relatively amorphous.[21a]

2.2. Optical and Electronic Properties

The UV-Vis absorption spectra of PIDTT-DFBT, PIDTT-DFBT-T, and PIDTT-DFBT-TT in solution and film are shown in **Figure 1** and the results are summarized in **Table 1**. In both solution and film, incorporation of the thiophene and TT π-bridge into PIDTT-DFBT results in the loss of the long wavelength absorption band (635 nm in solution and 647 nm in film), which was previously attributed to intramolecular charge transfer between the donor and acceptor moieties of PIDTT-DFBT.[21a] However, there is an enhanced absorption at the shorter wavelength bands at 437 and 580 nm for PIDTT-DFBT-T and 442 and 584 nm for PIDTT-DFBT-TT in films, accompanied by a significant broadening of the absorption bands. Although, this is a common effect of π-bridge incorporation in D–A polymers, it usually accompanied by a red-shift of the absorption bands due to increased intermolecular interactions from improved π-stacking resulting from greater planarity of the polymer backbone and an extended effective conjugation length.[22b] This is not the case with PIDTT-DFBT-T and PIDTT-DFBT-TT whose longer wavelength absorption bands actually blue-shifted slightly compared to PIDTT-DFBT. This may be the result of incorporating alkyl side-chains on the π-bridges that introduces unfavorable steric hindrance. Density functional theory calculated optimized geometries of dimers of the polymers (**Figure 2**) show much larger dihedral angles between the IDTT and the π-bridge (28° and 36° for IDTT-DFBT-T and IDTT-DFBT-TT, respectively, compared to 1° for IDTT-DFBT), providing evidence that the blue-shifted absorption of the T- and TT- bridged polymers is due to a decreased effective conjugation length in the more twisted π-bridged backbone. Despite possessing similar steric strain in the backbone, IDTT-DFBT-TT has a larger optical band-gap than IDTT-DFBT-TT (1.81 eV and 1.75 eV, respectively). The increased optical band-gap of IDTT-DFBT-TT is likely due to the increased aromaticity of theino[3,2-b]thiophene compared to thiophene, which results in decreased electron delocalization in the IDTT-DFBT-TT backbone.[25]

In order to determine the orbital energy levels of the polymers, cyclic voltammetry (CV) was employed to measure the

Table 1. Polymer Optical and Electronic Properties.

	M_n [kDa]	PDI	λ_{max}^{soln} [nm][a)]	λ_{max}^{film} [nm]	E_g^{opt} [eV]	HOMO [eV][b)]	LUMO [eV][b)]	E_g^{ec} [eV]
PIDTT-DFBT	24.0	2.6	635	647	1.78	–5.3	–3.5	1.8
PIDTT-DFBT-T	11.3	1.9	570	580	1.75	–5.3	–3.4	1.9
PIDTT-DFBT-TT	19.7	2.3	559	584	1.81	–5.3	–3.3	2.0

[a)]Measured in dilute chlorobenzene solutions; [b)]Calculated from the oxidation and reduction onset potentials after referencing to ferrocene using the equation $E_{HOMO/LUMO} = -4.8 - E_{onset}$.

© 2013 WILEY-VCH Verlag GmbH & Co. KGaA, Weinheim

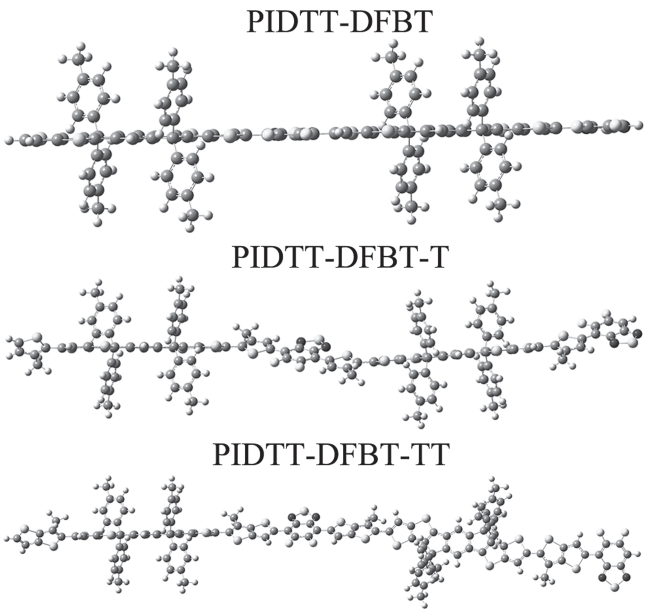

Figure 2. DFT calculated (B3LYP/6–31G*) optimized geometries of the polymers.

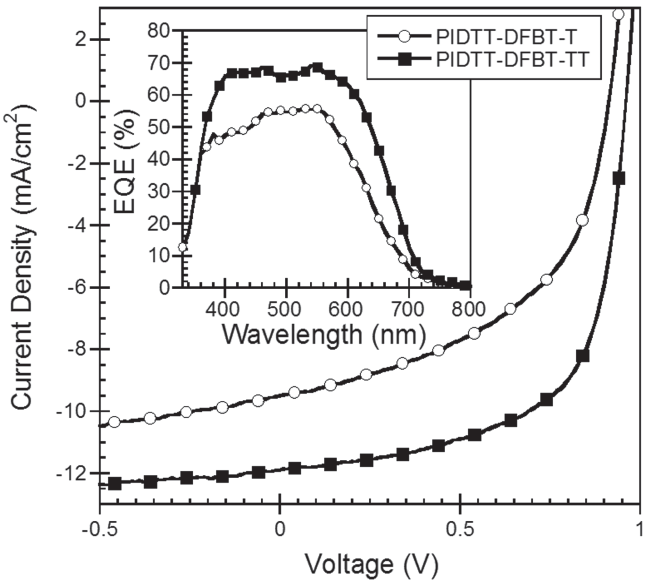

Figure 3. Characteristic *J–V* curves for the conventional solar cells derived from PIDT-DFBT-T and PIDTT-DFBT-TT. The inset shows the external quantum efficiency spectra for the BHJ devices.

red-ox potential of the polymers. The voltammograms can be seen in Figure S2 of the Supporting Information and the results are summarized in Table 1. The HOMO/LUMO energies for PIDTT-DFBT, PIDTT-DFBT-T, and PIDTT-DFBT-TT are –5.3/–3.5 eV, –5.3/–3.4 eV, –5.3/–3.3 eV, respectively. Incorporation of the π-bridges did not have much effect on the HOMO energy levels of the polymers but it affected the LUMO energy level. Both PIDTT-DFBT-T and PIDTT-DFBT-TT possess higher LUMO energy levels and larger band-gaps than PIDTT-DFBT, mirroring the decreasing planarity of the polymers.

2.3. Charge Carrier Mobilities

Charge mobilities of the polymers were investigated in organic field-effect transistors (OFET) with a bottom gate and top contact configuration. The results of the transfer curves are summarized in **Table 2**. PIDTT-DFBT-T shows a lower hole mobility (1.6×10^{-3} cm^2 V^{-1} s^{-1}) than that of PIDTT-DFBT (2×10^{-2} cm^2 V^{-1} s^{-1}).[21a] The decreased mobility is likely the result of the low molecular weight of PIDTT-DFBT-T.[26] Recently, DeLongchamp et al. reported that charge transport in amorphous ladder-type polymer films occurs primarily along the polymer backbone, with a minimum of intermolecular charge-hopping.[27] As a result, charge carrier mobility is directly related to the length of the polymer chain, and by extension, its molecular weight. Meanwhile, PIDTT-DFBT-TT exhibited a hole-mobility of 4.0×10^{-2} cm^2 V^{-1} s^{-1}, a slight improvement over PIDTT-DFBT. Both PIDTT-DFT-T and PIDTT-DFBT-TT showed primarily p-type characteristics, with very low electron mobilities that were three orders of magnitude lower than that of PIDT-DFBT.

2.4. Conventional Photovoltaic Cells

The performance of the new polymers was first evaluated in solar cells with a conventional configuration of ITO/PEDOT:PSS/polymer:$PC_{71}BM$(1:3)/Bis-C_{60}/Ag (details in the Supporting Information). **Figure 3** shows the *J–V* curves of the devices with PIDTT-DFBT-T:$PC_{71}BM$ and PIDTT-DFBT-TT:$PC_{71}BM$ active layers and the performance of these devices is summarized in Table 2.

As mentioned previously, incorporation of the π-bridges led to the loss of the low energy intramolecular charge transfer absorption band of PIDTT-DFBT, but with enhanced absorption at shorter wavelengths from the individual moieties of the polymers. Despite this loss of absorption in the peak intensity region of the solar spectrum, the polymers still showed high performance in OPVs. The devices based on PIDTT-DFBT-T exhibited a PCE of 4.4% with a V_{OC} of 0.91 V, a short-circuit current density (J_{SC}) of 9.5 mA cm^{-2} and a fill-factor (FF) of 0.50. These results are substantially lower than that reported for PIDTT-DFBT.[21a] In contrast, the PIDTT-DFBT-TT-based devices showed an improved PCE of 7.2%, compared to PIDTT-DFBT with a V_{OC} of 0.96 V, a J_{SC} of 11.9 mA cm^{-2}, and a FF of 0.63. The reduced performance of PIDTT-DFBT-T can be attributed to

Table 2. Device Characteristics of OFETs and Conventional OPVs.

Polymer	$\mu_{sat,h}$ [cm^2 V^{-1} s^{-1}]	$I_{on}/I_{off,h}$	$\mu_{sat,e}$ [cm^2 V^{-1} s^{-1}]	$I_{on}/I_{off,e}$	V_{OC} [V]	J_{SC} [mA cm^{-2}]	FF [%]	η [%]
PIDTT-DFBT-T	1.6×10^{-3}	1.6×10^{4}	1.7×10^{-5}	6.0×10^{3}	0.91	9.5	50	4.4
PIDTT-DFBT-TT	4.0×10^{-2}	1.4×10^{5}	2.5×10^{-5}	3.6×10^{6}	0.96	11.9	63	7.2

© 2013 WILEY-VCH Verlag GmbH & Co. KGaA, Weinheim

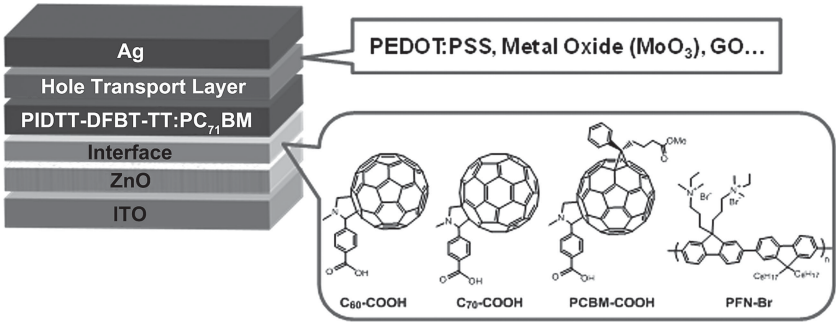

Figure 4. The device structure of the inverted PIDTT-DFBT-TT:$PC_{71}BM$ solar cell. Inset shows the molecular structures of ZnO modification materials and various hole transporting layers.

the low molecular weight of the polymer, which led to decreased charge carrier mobility. The decreased hole-mobility resulted in lower J_{SC} and FF for PIDTT-DFBT-T compared to the other polymers. PIDTT-DFBT-TT, on the other hand, possessed a slightly higher hole-mobility than PIDTT-DFBT, which led to an improved FF, and despite its disadvantageous absorption, still exhibits a comparably high PCE to that of PIDTT-DFBT.

The improved FF could also be due to an improved film morphology, however, AFM height and phase images of polymer-fullerene blend surfaces (Figure S3, Supporting Information) showed a similar surface morphology as PIDTT-DFBT with a root-mean-square (RMS) roughness of 0.93 nm for PIDTT-DFBT-TT, versus the reported RMS value of 0.92 for PIDTT-DFBT. The high performance of PIDTT-DFBT-TT-based devices, coupled with its enhanced absorption at shorter wavelengths, suggests it could be a good candidate as a large band-gap material for tandem solar cells. Because large band-gap polymers in tandem cells typically are fabricated in an inverted structure, PIDTT-DFBT-TT was also evaluated in inverted devices to guage its potential.

2.5. Inverted Photovoltaic Cells

The inverted devices were first evaluated by modifying the anode with a variety of interfacial layers in order to optimize device performance, including the use of fullerene-based self-assembled monolayers (SAM) (C_{60}-COOH, C_{70}-COOH and PCBM-COOH) and PFN-Br surfactant on top of ZnO (as shown in **Figure 4**) to function as an interfacial layer to facilitate electron transport and extraction. Preparative details are described in the SI. Photovoltaic characteristics were first investigated with the device architectures of ITO/ZnO/PIDTT-DFBT-TT:$PC_{71}BM$/MoO_3/Ag and ITO/ZnO/C_{60}-COOH/PIDTT-DFBT-TT:$PC_{71}BM$/MoO_3/Ag. The effect of the ZnO modification is shown in the Supporting Information, Figure S4 and Table S1.

The application of the SAM reduces the device series resistance by passivating the inorganic surface traps as well as enhances the electronic coupling at the ZnO-organic interface.[18] Without any interfacial layer, inverted OPVs showed a J_{SC} of 9.5 mA cm^{-2}, a *Voc* of 0.73 V, a *FF* of 0.44 and a corresponding PCE of 3.1%. After introducing a C_{60}-COOH SAM onto the ZnO layer, inverted OPVs showed a *Jsc* of 11.4 mA cm^{-2}, a V_{OC} of 0.94 V, a *FF* of 51% and a corresponding PCE of 5.4%, nearly a 70% enhancement in the PCE. At the same time, PFN-based surfactant can also be used to modify the ZnO electron extraction layer. The increased V_{OC} and *FF* indicated that the conjugated polymer interfacial layer can lower the work function and decrease the series resistance.[6c] Interestingly, when PCBM-COOH was used instead, the observed V_{OC} increased to 0.94 V, due to the matching LUMO level between the PCBM-COOH SAM and the $PC_{71}BM$ acceptors in the active layer.

Although the PCBM-COOH SAM modified ZnO layer acts as a good electron extraction layer, its device performance is still inferior compared to the optimized conventional devices in the PIDTT-DFBT-TT-based cells, implying there is still room for improvement. at the anode side, many inverted BHJ solar cells have been reported with an interlayer of wet processed PEDOT:PSS to replace the thermally evaporated transition metal oxide.[28] However, the aqueous dispersed PEDOT:PSS is difficult to coat onto an organic active layer due the hydrophobicity of organic polymers,[29] especially for the fluoropolymer PIDTT-DFBT-TT.

As an alternative to PEDOT:PSS, graphene oxide (GO) has been used as an efficient hole extraction layer.[30] GO is a derivative of graphene that is prepared by chemical oxidation of naturally abundant graphite.[31] The presence of functional groups, such as carboxyl, hydroxyl, and epoxy groups, gives rise to proton dissociation, leading to surface doping at the GO/polymer interface, improving conductivity.[32] In fact, we have previously found that the unique 2D structure of GO prohibits it from penetrating into the bulk-heterojunction, making it an ideal material for surface doping. The heavily doped interface, with higher conductivity, facilitates the formation of an Ohmic contact between the active layer and the top metal electrode.[33] Additionally, the high-lying E_{LUMO} of graphene oxide (GO) allows the material to act as an effective electron blocking interlayer.[34] When MoO_3 is replaced with GO, an improved PCE of 5.5% is obtained due to an enhanced V_{OC} and J_{SC} (**Figure 5**a). However, a thin GO film did not bring the significant enhancement of the results due to its limited electron-blocking ability.[35] To further improve the anode contact, a hybrid bilayer interfacial material based on GO/MoO_3 was developed. Interestingly, there is a synergistic effect in BHJ solar cells when the GO and MoO_3 are sequentially spin-coated and deposited on top of the BHJ. Interestingly, the device based on the hybrid GO/MoO_3 interfacial layer exhibits an improved PCE of 6.4% with an enhanced FF and V_{OC}.

To futher clarify the function of GO, a series of mophological and electronic analyses of the HTLs in the devices were studied. The surface morphologies of the different HTLs on top of the PIDTT-DFBT-TT:$PC_{71}BM$ active layer were examined by atomic force microscopy (AFM) and their topography images are shown in Figure S5, Supporting Information. Figures S5c,d show the topography images of the MoO_3 and GO/MoO_3 layer processed onto the active layer, respectively. The AFM images clearly show that the MoO_3 has a much smoother surface when deposited onto GO instead of the active layer, as the RMS roughness of the MoO_3 layer imporves from 1.92 to 1.62 nm. As a result, the more homogenious interface

© 2013 WILEY-VCH Verlag GmbH & Co. KGaA, Weinheim

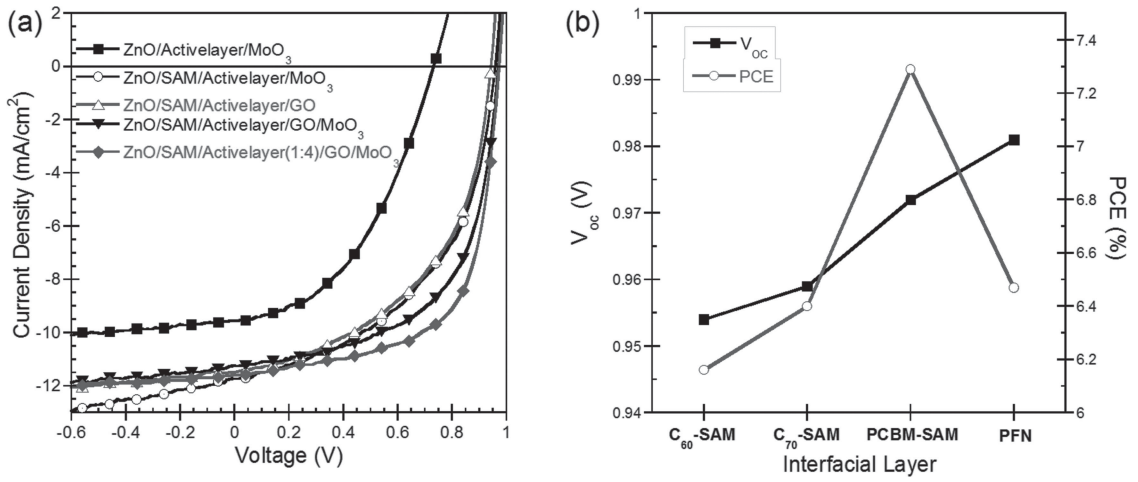

Figure 5. a) *J– V* characteristics of inverted structure device based on PIDTT-DFBT-TT:$PC_{71}BM$ (1:3) with different hole transporting layers, as well as the optimized device using a PIDTT-DFBT-TT:$PC_{71}BM$ ratio of 1:4. b) Plots comparing the effect of four different ZnO modifications on the V_{OC} and PCE of the inverted device ITO/ZnO/interface/PIDTT-DFBT-TT:$PC_{71}BM$ (1:4)/GO/MoO_3/Ag.

between the hybrid GO/MoO_3 HTL and top electrode reduces the series resistance and thus improves the FF, as observed in the devices. This improvent could also be seen in the dark current of the corresponding devices. Figure S6 (Supporting Information) shows that the device derived from the hybrid HTL has a dark current that is an order of magnitude smaller under reverse bias than the control device without GO, while both devices exhibit similar current in the forward direction. The lower dark current densities indicate that the leakage was suppressed by the introduction of the GO layer, which apparently benefits from the more uniform interface between GO/MoO_3 and electrode.

As summarized in **Table 3**, the V_{OC} of the device with the GO interfacial layer is larger than the value of the device without GO. This indicates that the built-in voltage (V_{BI}) may be enhanced after the incorporation of the GO layer. To further explore the influences of GO on the surface electronic states in PIDTT-DFBT-TT:$PC_{71}BM$ active layers, and on the subsequent device performance, capacitance–voltage (*C–V*) characterization was conducted and examined through Mott–Schottky (MS) analysis.[36] The values of V_{BI} were estimated by the voltage corresponding to the maxima of capacitance which equals the flat-band condition, while the band-bending results allow for extraction of the impurity concentration (*N*) of the region by application of $C^{-2} = (2/q\varepsilon N)(V_{BI} - V)$ to the appropriate bias voltage range.[37] *C–V* characteristics of the devices using MoO_3 or GO/MoO_3 as the HTL were obtained by applying a low AC perturbation signal with a fixed frequency and sweeping the DC bias.[38] As shown in **Figure 6**a, an estimated V_{BI} of 0.95 ± 0.05 V was obtained for the MoO_3 control device, with a maximum value of *N* of (2.51 ± 1.12) × 10^{16} cm^{-3}, which roughly defines the upper limit for the open voltage for this device.

For the device using the hole-transporting GO/MoO_3 hybrid HTL, both V_{BI} and *N* are noticably increased after the introduction of the GO. The estimated V_{BI} is 1.02 ± 0.05 V and the maximum value of *N* increases to around (3.93 ± 1.35) × 10^{16} cm^{-3}. The observed changes in V_{BI} are reflected in the magnitude of the change in V_{OC}. Additionally, the increase in the N value

Table 3. Inverted device characteristics of PIDTT-DFBT-TT:$PC_{71}BM$ with different hole transporting layer of GO, MoO_3, and GO/MoO_3, with and without PCBM-COOH SAM modification on ZnO.

Device	*Jsc* [mA cm^{-2}]	*Voc* [mV]	*FF* [%]	η [%]
ITO/ZnO/Activelayer(1:3)/MoO3/Ag	9.5	731	44.3	3.08
ITO/ZnO/PCBM-COOH/ Activelayer(1:3)/MoO3/Ag	11.4	942	50.5	5.42
ITO/ZnO/PCBM-COOH/ Activelayer(1:3)/GO/Ag	11.6	958	49.3	5.50
ITO/ZnO/PCBM-COOH/ Activelayer(1:3)/GO/MoO3/Ag	11.2	969	59.0	6.38
ITO/ZnO/PCBM-COOH/ Activelayer(1:4)/GO/MoO3/Ag	11.6	972	64.5	7.29

suggests the GO layer could increase the surface charge density, probably due to the diminishment of surface traps. This result is consistent with the observation in the aforementioned morphological analysis, in which the GO/MoO_3 hybrid HTL provides a more continuous surface than the MoO_3 only HTL. On the other hand, the surface doping and the increased conductivity of the interface between active layer and metal electrode from using GO may also contribute to the enhanced V_{BI} and *N*. Moreover, with the enhancement in V_{OC}, an simultaneous increase in FF is also observed with a FF of optimized devices found to be 59.0%, which is much higher than that of the control devices (50.5%). The improved homogeneous surface of the hybrid HTL reduces the resistance between BHJ and HTL, while the surface doping improves conductivity, facilitating the charge colleciton. Accordingly, the effects of the GO layer on the charge-transport properties were further investigated by examining the hole mobilities of the inverted device using the space-charge limited current (SCLC) model. The detailed fabrication and analysis are described in the Supporting Information (Figure S7). Hole mobilities of 3.7 × 10^{-4} cm^2 V^{-1} s^{-1} and 1.5 × 10^{-3} cm^2 V^{-1} s^{-1} were observed for the device using

© 2013 WILEY-VCH Verlag GmbH & Co. KGaA, Weinheim

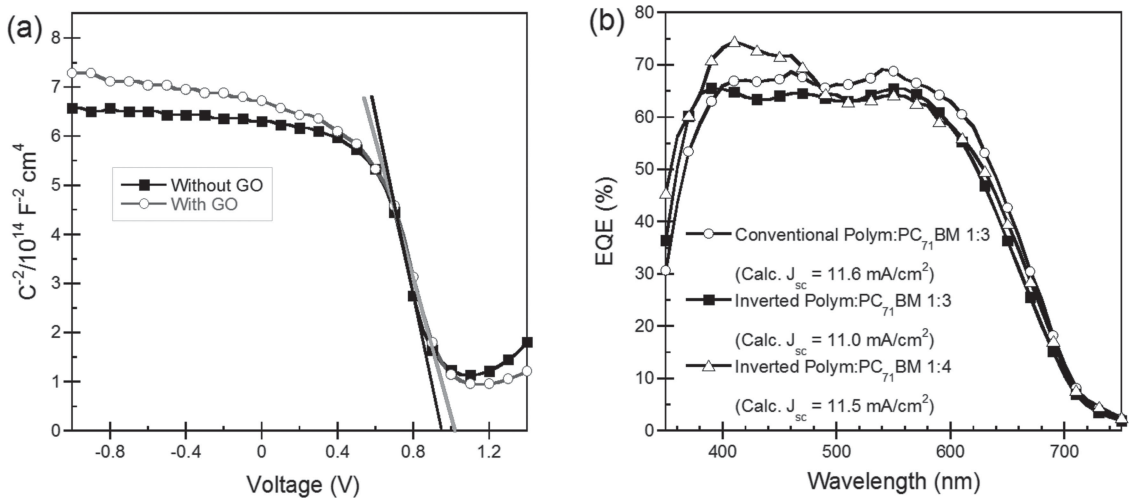

Figure 6. a) Impedance spectra analysis for the effect of GO layer on the inverted solar cell. C^{-2} versus applied bias voltage with MoO_3 only HTL or GO/MoO_3 combined HTL. The straight lines correspond to the Mott–Schottky plot. b) EQE of devices based on conventional and inverted structure with PIDTT-DFBT-TT:PC_{71}BM blending ratios of 1:3 and 1:4.

MoO3 and GO/MoO3 as the hole transporting layer, respectively. The increased hole mobility confirms the improved interfacial charge transport from the hybrid HTL. The use of this new hybrid hole transporting layer does not directly change the energy levels of active materials and their band gap, leaving light absorption unaffected. Therefore, the trade-off between V_{OC} and J_{SC} can be avoided. This strategy coincides well with a recent study by Hsu and co-workers, who reported a novel solution processed GO/VO*x* hybird HTL.[39]

The effect of device geometry on exciton generation and overall performance have been previously investigated in detail using the optical field distribution and exciton generation profiles in inverted devices based on the use of IDT-PhanQ polymer and PC_{71}BM as the active layer.[40] In order to maintain adequate electron mobility and achieve optimal PCE, higher fullerene blending ratio (1:4) is needed in these inverted devices. The same approach has been applied to our current material system with the only difference being in the interfacial layers used to modify the ZnO layer (see Figure S8 and Table S3 in the Supporting Information). The variations in V_{OC} and PCE from the different ZnO processing conditions are shown in Figure 6b. Similar to our previous study, the best performance was achieved for devices with a 1:4 ratio of PIDTT-DFBT-TT and PCBM as the active layer, a PCBM-COOH SAM modified ZnO layer, and GO/MoO_3 as the ETL and HTL, respectively. The best device exhibited a J_{SC}, V_{OC}, FF, and PCE of 11.6 mA cm^{-2}, 0.97 V, 64.5%, and 7.3%, respectively. After the fine-tuning of the active layer thickness (see Figure S9 of the Supporting Information), the device performance is comparable to or even slightly better than those obtained from the conventional device configuration. The slight increase in performance can be attributed by the difference in absorption of the devices. Compared to the EQE spectra of the inverted solar cells with 1:3 and 1:4 polymer:fullerene blending ratios, the films with 1:3 ratio showed similar EQE in the range between 500 and 650 nm, while the films with a 1:4 ratio gained higher EQE in the rangesof 350–500 nm. These results show that an inverted device can perform equal to or better than the conventional device if each component of the device is optimized.

3. Conclusion

In summary, highly efficient inverted solar cells were made through careful engineering of materials and devices. Optimum material properties were realized through incorporation of an octylthieno[3,2-b]thiophene π-bridge between an IDTT donor and DFBT acceptor. The π-bridge led to enhanced shorter wavelength absorption of the polymer, while maintaining a high hole mobility and photovoltaic performance. Inverted solar cells made from this material initially showed poor performance, however, after the incorporation of a fullerene-SAM modified ZnO as the ETL and a GO/MoO_3 bilayer as the HTL, the device showed significantly improved V_{OC}, J_{SC}, and FF which resulted in a high PCE of 7.3% in optimized devices.

4. Experimental Section

Materials and Characterization: All chemicals were purchased from Aldrich and used without purification. 4,7-dibromo-5,6-difluoro-[2,1,3] benzothiadiazole,[41] 4-hexyl-2-trimethylstannylthiophene,[42] 6-octyl-2-trimethylstanylthieno[3,2-*b*]thiophene,[43] the monomer IDTT,[21a] and the polymer PIDTT-DFBT[21a] were made according to literature procedures. DFBT-T and DFBT-TT were prepared according to the procedures described in the supporting information. Graphene oxide was prepared by the modified Hummer's method from natural flake graphite.[31] UV-Vis spectra were measured using a Perkin-Elmer Lambda-9 spectrophotometer. The ^{1}H and ^{13}C NMR spectra were collected on a Bruker AV300 and AV500 spectrometers operating at 300 and 125 MHz, respectively, in deuterated chloroform solution referenced to TMS. Mass spectrometry data was collected on a Bruker Esquire mass spectrometer with a quadrupole ion trap, using electrospray ionization. GPC measurements were performed on a Waters GPC using a 1515 isocratic pump and refractive index detector with an tetrahydrofuran mobile phase at 35 °C. Thermal transitions were measured on a TA Instruments Q20–1066 Differential Scanning Calorimeter with a heating rate of

© 2013 WILEY-VCH Verlag GmbH & Co. KGaA, Weinheim

10 °C min^{-1}. Cyclic voltammetry of polymer films was conducted in acetonitrile with 0.1 m tetrabutylammonium hexafluorophosphate using a scan rate of 100 mV s^{-1}. A platinum button, Ag/AgCl and Pt mesh were used as the working electrode, reference electrode, and counter electrode, respectively. AFM images under tapping mode were taken on a Veeco multimode AFM with a Nanoscope III controller.

Device Fabrication: OPVs were fabricated using ITO-coated glass substrates (15 Ω sq^{-1}), which were cleaned with detergent, deionized water, acetone, and isopropyl alcohol. In the conventional structure devices, a thin layer (≈35 nm) of PEDOT:PSS (Baytron P VP AI 4083, filtered at 0.45 μm) was first spin-coated on the pre-cleaned ITO-coated glass substrates at 5000 rpm and baked at 140 °C for 10 min under ambient conditions. The substrates were then transferred into a nitrogen filled glovebox. Subsequently, the polymer:PC_{71} BM active layer (≈90 nm) was spin-coated on the PEDOT:PSS layer from a homogeneous solution. The solution was prepared by dissolving the polymer and fullerene at different weight ratios in o-dichlorobenzene overnight and filtered through a PTFE (polytetrafluoroethylene) filter (0.45 μm). Fullerene surfactant layer was further spun onto the active layer and then thermally annealed at 110 °C for 5 min. Finally, Ag (100 nm) were thermally evaporated under high vacuum (< 2×10^{-6} Torr) to serve as the cathode. As for the inverted structure, the prepared ZnO sol–gel was spin-coated on the pre-cleaned ITO-coated glass substrate at 4000 rpm. The ZnO films were annealed at 200 °C for 1 h in the air. Different SAM (C60-COOH, C70-COOH, and PCBM-COOH) was deposited on the ZnO surface using a two-step spin process.[18] For ZnO modified with PFN-Br as an electron extraction layer, an approximately 5 nm thick PFN-Br layer was cast on top of ZnO films.[6c] Afterward, the same process used for the active layer in the conventional structure devices was also used for the inverted devices. After annealing, 7 nm MoO_3 and 100 nm Ag were deposited sequentially under high vacuum by thermal evaporation. All the *J–V* curves in this study were recorded using a Keithley 2400 source measure unit. The device photocurrent was measured under illumination from a 450 W Thermal Oriel solar simulator (AM 1.5G). The illumination intensity of the light source was accurately calibrated employing a standard Si photodiode detector equipped with a KG-5 filter, which can be traced back to the standard cell of National Renewable Energy Laboratory (NREL). The calibration method, based on the IEC-69094–1 spectrum, followed procedures described previously. The EQE spectra performed here are obtained by the IPCE measurement using the combination of a Xenon lamp (Oriel, 450 W) as the light source, a monochromator, chopper with frequency of 100Hz, a lock-in amplifier (SR830, Stanford Research Corp), and a Si-based diode (J115711–1-Si detector) for calibration.

Polymerization of PIDTT-DFBT-T: IDTT (65 mg, 0.048 mmol) and DFBT-T (32 mg, 0.048 mmol) were dissolved in toluene (10 mL) and DMF (0.1 mL). The mixture was purged with argon for 30 min, then $Pd_2(dba)_3$ (0.0024 mmol) and $P(o\text{-}tol)_3$ (0.0087 mmol) were added. The mixture was then refluxed for 48 h. After cooling to room temperature, the polymer was precipitated into methanol and filtered. The collected precipitate was subjected to Soxhlet extraction with methanol, hexanes, and chloroform. The chloroform extract was concentrated and then precipitated into methanol. The polymer was then filtered and dried under vacuum to yield a purple solid (62 mg, 85% yield). ^{1}H NMR (500 MHz, CDCl3, δ): 8.13(s, 2H), 7.53(s, 2H), 7.46(s, 2H), 7.24 (m, 8H), 7.12(m, 8H), 2.86 (m, 4H), 2.57 (m, 8H), 1.73 (m, 4H), 1.72–1.60 (m, 8H), 1.51–1.43 (m, 12H), 1.34–1.28 (m, 24H), 1.03 (m, 6H), 0.86 (m, 12H). GPC (THF): M_n = 11.3 kDa, M_w = 21.5 kDa, PDI = 1.9.

Polymerization of PIDTT-DFBT-TT: IDTT (212 mg, 0.16 mmol) and DFBT-TT (125 mg, 0.15 mmol) were dissolved in toluene (5 mL) and deoxygenated by bubbling nitrogen through the mixture for 30 min. $Pd_2(dba)_3$ (2.7 mg, 3 μmol) and tri-o-tolylphosphine (3.7 mg, 12 μmol) were added and the mixture was heated to a reflux under nitrogen for 3 days. A drop of 2-trimethylstannylthiophene was added and the mixture continued to reflux for 3 h. Two drops of 2-bromothiophene were then added and the mixture was refluxed overnight. After cooling to room temperature, the mixture was poured into methanol and the precipitate was collected and then washed in a Soxhlet extractor with acetone and hexane. The remaining polymer was dissolved in chloroform and precipitated into methanol. The solid was then filtered and dried to yield a purple solid (244 mg, 96% yield). ^{1}H NMR (300 MHz, $CDCl_3$, δ): 8.55 (s, 2H), 7.57 (s, 2H), 7.43 (s, 2H), 7.26 (d, J = 8.4 Hz, 8H), 7.15 (d, J = 8.0 Hz, 8H), 2.60 (m, 12H), 1.59–1.62 (m, 12H), 1.25–1.37 (m, 44H), 0.87–0.91 (m, 18H); GPC (THF): M_n = 19.7 kDa, M_w = 45.3 kDa, PDI = 2.3.

Supporting Information

Supporting Information is available from Wiley Online Library or from the author.

Acknowledgements

J.J.I. and K.Y. contributed equally to this work. The authors thank the support from the National Science Foundation (DMR-0120967), the Air Force Office of Scientific Research (FA9550–09–1–0426), the Asian Office of Aerospace R&D (FA2386–11–1–4072), and the Office of Naval Research (N00014–11–1–0300). A.K.-Y.J. thanks the Boeing Foundation for support.

Received: July 18, 2013
Revised: September 9, 2013
Published online: October 14, 2013

[1] a) Y.-J. Cheng, S.-H. Yang, C.-S. Hsu, *Chem. Rev.* **2009**, *109*, 5868; b) I. McCulloch, R. S. Ashraf, L. Biniek, H. Bronstein, C. Combe, J. E. Donaghey, D. I. James, C. B. Nielsen, B. C. Schroeder, W. Zhang, *Acc. Chem. Res.* **2012**, *45*, 714; c) C. Duan, F. Huang, Y. Cao, *J. Mater. Chem.* **2012**, *22*, 10416.

[2] a) H.-L. Yip, A. K. Y. Jen, *Energy Environ. Sci.* **2012**, *5*, 5994; b) H. Ma, H.-L. Yip, F. Huang, A. K. Y. Jen, *Adv. Funct. Mater.* **2010**, *20*, 1371; c) S. Sista, M.-H. Park, Z. Hong, Y. Wu, J. Hou, W. L. Kwan, G. Li, Y. Yang, *Adv. Mater.* **2010**, *22*, 380; d) C.-Z. Li, H.-L. Yip, A. K. Y. Jen, *J. Mater. Chem.* **2012**, *22*, 4161.

[3] a) X. Hu, M. Wang, F. Huang, X. Gong, Y. Cao, *Synth. Met.* **2013**, *164*, 1; b) J. K. Lee, W. L. Ma, C. J. Brabec, J. Yuen, J. S. Moon, J. Y. Kim, K. Lee, G. C. Bazan, A. J. Heeger, *J. Am. Chem. Soc.* **2008**, *130*, 3619; c) C. V. Hoven, X.-D. Dang, R. C. Coffin, J. Peet, T.-Q. Nguyen, G. C. Bazan, *Adv. Mater.* **2010**, *22*, E63.

[4] a) C.-Y. Chang, Y.-J. Cheng, S.-H. Hung, J.-S. Wu, W.-S. Kao, C.-H. Lee, C.-S. Hsu, *Adv. Mater.* **2012**, *24*, 549; b) F. C. Krebs, S. A. Gevorgyan, J. Alstrup, *J. Mater. Chem.* **2009**, *19*, 5442; c) F. Zhang, X. Xu, W. Tang, J. Zhang, Z. Zhuo, J. Wang, J. Wang, Z. Xu, Y. Wang, *Sol. Energy Mater. Sol. Cells* **2011**, *95*, 1785.

[5] a) J. Y. Kim, K. Lee, N. E. Coates, D. Moses, T.-Q. Nguyen, M. Dante, A. J. Heeger, *Science* **2007**, *317*, 222; b) L. Dou, J. You, J. Yang, C.-C. Chen, Y. He, S. Murase, T. Moriarty, K. Emery, G. Li, Y. Yang, *Nat. Photonics* **2012**, *6*, 180; c) T. Ameri, G. Dennler, C. Lungenschmied, C. J. Brabec, *Energy Environ. Sci.* **2009**, *2*, 347; d) G. Dennler, M. C. Scharber, T. Ameri, P. Denk, K. Forberich, C. Waldauf, C. J. Brabec, *Adv. Mater.* **2008**, *20*, 579.

[6] a) Z. He, C. Zhong, S. Su, M. Xu, H. Wu, Y. Cao, *Nat. Photonics* **2012**, *6*, 591; b) H.-C. Chen, Y.-H. Chen, C.-C. Liu, Y.-C. Chien, S.-W. Chou, P.-T. Chou, *Chem. Mater.* **2012**, *24*, 4766; c) T. Yang, M. Wang, C. Duan, X. Hu, L. Huang, J. Peng, F. Huang, X. Gong, *Energy Environ. Sci.* **2012**, *5*, 8208; d) Z. He, C. Zhong, X. Huang, W.-Y. Wong, H. Wu, L. Chen, S. Su, Y. Cao, *Adv. Mater.* **2011**, *23*, 4636; e) C. E. Small, S. Chen, J. Subbiah, C. M. Amb, S.-W. Tsang, T.-H. Lai, J. R. Reynolds, F. So, *Nat. Photonics* **2012**, *6*, 115.

[7] J. You, L. Dou, K. Yoshimura, T. Kato, K. Ohya, T. Moriarty, K. Emery, C.-C. Chen, J. Gao, G. Li, Y. Yang, *Nat. Commun.* **2013**, *4*, 1446.

© 2013 WILEY-VCH Verlag GmbH & Co. KGaA, Weinheim

[8] a) H. Park, K. Y. Lee, W. Kim, H.-W. Shin, D. H. Wang, T. K. Ahn, J. H. Park, *ACS Appl. Mater. Interfaces* **2013**, *5*, 1612; b) F. C. Krebs, K. Norrman, *Prog. Photovoltaics Res. Appl.* **2007**, *15*, 697; c) J. A. Hauch, P. Schilinsky, S. A. Choulis, R. Childers, M. Biele, C. J. Brabec, *Sol. Energy Mater. Sol. Cells* **2008**, *92*, 727.

[9] a) K. Kawano, R. Pacios, D. Poplavskyy, J. Nelson, D. D. C. Bradley, J. R. Durrant, *Sol. Energy Mater. Sol. Cells* **2006**, *90*, 3520; b) M. O. Reese, A. J. Morfa, M. S. White, N. Kopidakis, S. E. Shaheen, G. Rumbles, D. S. Ginley, *Sol. Energy Mater. Sol. Cells* **2008**, *92*, 746.

[10] C.-P. Chen, Y.-D. Chen, S.-C. Chuang, *Adv. Mater.* **2011**, *23*, 3859.

[11] M. D. Irwin, D. B. Buchholz, A. W. Hains, R. P. H. Chang, T. J. Marks, *Proc. Natl. Acad. Sci. U. S. A.* **2008**, *105*, 2783.

[12] J. J. Jasieniak, J. Seifter, J. Jo, T. Mates, A. J. Heeger, *Adv. Funct. Mater.* **2012**, *22*, 2594.

[13] Y. Sun, J. H. Seo, C. J. Takacs, J. Seifter, A. J. Heeger, *Adv. Mater.* **2011**, *23*, 1679.

[14] Y.-J. Cheng, F.-Y. Cao, W.-C. Lin, C.-H. Chen, C.-H. Hsieh, *Chem. Mater.* **2011**, *23*, 1512.

[15] L.-M. Chen, Z. Xu, Z. Hong, Y. Yang, *J. Mater. Chem.* **2010**, *20*, 2575.

[16] R. Po, C. Carbonera, A. Bernardi, N. Camaioni, *Energy Environ. Sci.* **2011**, *4*, 285.

[17] L.-L. Chua, J. Zaumseil, J.-F. Chang, E. C. W. Ou, P. K. H. Ho, H. Sirringhaus, R. H. Friend, *Nature* **2005**, *434*, 194.

[18] S. K. Hau, H.-L. Yip, H. Ma, A. K. Y. Jen, *Appl. Phys. Lett.* **2008**, *93*, 233304.

[19] A. K. K. Kyaw, D. H. Wang, V. Gupta, J. Zhang, S. Chand, G. C. Bazan, A. J. Heeger, *Adv. Mater.* **2013**, *25*, 2397.

[20] a) Y. Huang, X. Guo, F. Liu, L. Huo, Y. Chen, T. P. Russell, C. C. Han, Y. Li, J. Hou, *Adv. Mater.* **2012**, *24*, 3383; b) S. Qu, H. Tian, *Chem. Commun.* **2012**, *48*, 3039; c) M. Wang, X. Hu, P. Liu, W. Li, X. Gong, F. Huang, Y. Cao, *J. Am. Chem. Soc.* **2011**, *133*, 9638.

[21] a) Y.-X. Xu, C.-C. Chueh, H.-L. Yip, F.-Z. Ding, Y.-X. Li, C.-Z. Li, X. Li, W.-C. Chen, A. K. Y. Jen, *Adv. Mater.* **2012**, *24*, 6356; b) H.-H. Chang, C.-E. Tsai, Y.-Y. Lai, D.-Y. Chiou, S.-L. Hsu, C.-S. Hsu, Y.-J. Cheng, *Macromolecules* **2012**, *45*, 9282.

[22] a) X. Guo, S. R. Puniredd, M. Baumgarten, W. Pisula, K. Müllen, *J. Am. Chem. Soc.* **2012**, *134*, 8404; b) X. Wang, Y. Sun, S. Chen, X. Guo, M. Zhang, X. Li, Y. Li, H. Wang, *Macromolecules* **2012**, *45*, 1208.

[23] N. S. Baek, S. K. Hau, H.-L. Yip, O. Acton, K.-S. Chen, A. K. Y. Jen, *Chem. Mater.* **2008**, *20*, 5734.

[24] J. K. Park, J. Jo, J. H. Seo, J. S. Moon, Y. D. Park, K. Lee, A. J. Heeger, G. C. Bazan, *Adv. Mater.* **2011**, *23*, 2430.

[25] Y.-J. Cheng, S.-W. Cheng, C.-Y. Chang, W.-S. Kao, M.-H. Liao, C.-S. Hsu, *Chem. Commun.* **2012**, *48*, 3203.

[26] a) M. Tong, S. Cho, J. T. Rogers, K. Schmidt, B. B. Y. Hsu, D. Moses, R. C. Coffin, E. J. Kramer, G. C. Bazan, A. J. Heeger, *Adv. Funct. Mater.* **2010**, *20*, 3959; b) A. M. Ballantyne, L. Chen, J. Dane, T. Hammant, F. M. Braun, M. Heeney, W. Duffy, I. McCulloch, D. D. C. Bradley, J. Nelson, *Adv. Funct. Mater.* **2008**, *18*, 2373; c) J.-F. Chang, J. Clark, N. Zhao, H. Sirringhaus, D. W. Breiby, J. W. Andreasen, M. M. Nielsen, M. Giles, M. Heeney, I. McCulloch, *Phys. Rev. B: Condens. Matter Mater. Phys.* **2006**, *74*, 115318; d) J. J. Intemann, K. Yao, H.-L. Yip, Y.-X. Xu, Y.-X. Li, P.-W. Liang, F.-Z. Ding, X. Li, A. K. Y. Jen, *Chem. Mater.* **2013**, *25*, 3188.

[27] X. Zhang, H. Bronstein, A. J. Kronemeijer, J. Smith, Y. Kim, R. J. Kline, L. J. Richter, T. D. Anthopoulos, H. Sirringhaus, K. Song, M. Heeney, W. Zhang, I. McCulloch, D. M. DeLongchamp, *Nat. Commun.* **2013**, DOI: 10.1038/ncomms3238.

[28] R. Steim, F. R. Kogler, C. J. Brabec, *J. Mater. Chem.* **2010**, *20*, 2499.

[29] F. J. Lim, K. Ananthanarayanan, J. Luther, G. W. Ho, *J. Mater. Chem.* **2012**, *22*, 25057.

[30] J. Liu, Y. Xue, Y. Gao, D. Yu, M. Durstock, L. Dai, *Adv. Mater.* **2012**, *24*, 2228.

[31] Y. Zhu, S. Murali, W. Cai, X. Li, J. W. Suk, J. R. Potts, R. S. Ruoff, *Adv. Mater.* **2010**, *22*, 3906.

[32] Z. Wei, M. Wan, T. Lin, L. Dai, *Adv. Mater.* **2003**, *15*, 136.

[33] Y. Gao, H.-L. Yip, K.-S. Chen, K. M. O'Malley, O. Acton, Y. Sun, G. Ting, H. Chen, A. K. Y. Jen, *Adv. Mater.* **2011**, *23*, 1903.

[34] S.-S. Li, K.-H. Tu, C.-C. Lin, C.-W. Chen, M. Chhowalla, *ACS Nano* **2010**, *4*, 3169.

[35] B. R. Lee, J.-w. Kim, D. Kang, D. W. Lee, S.-J. Ko, H. J. Lee, C.-L. Lee, J. Y. Kim, H. S. Shin, M. H. Song, *ACS Nano* **2012**, *6*, 2984.

[36] G. Garcia-Belmonte, A. Guerrero, J. Bisquert, *J. Phys. Chem. Lett.* **2013**, *4*, 877.

[37] P. P. Boix, M. M. Wienk, R. A. J. Janssen, G. Garcia-Belmonte, *J. Phys. Chem. C* **2011**, *115*, 15075.

[38] K. M. O'Malley, C.-Z. Li, H.-L. Yip, A. K. Y. Jen, *Adv. Energy Mater.* **2012**, *2*, 82.

[39] Y.-H. Chao, J.-S. Wu, C.-E. Wu, J.-F. Jheng, C.-L. Wang, C.-S. Hsu, *Adv. Energy Mater.* **2013**, DOI: 10.1002/aenm.201300430.

[40] J. Zou, H.-L. Yip, Y. Zhang, Y. Gao, S.-C. Chien, K. O'Malley, C.-C. Chueh, H. Chen, A. K. Y. Jen, *Adv. Funct. Mater.* **2012**, *22*, 2804.

[41] Y. Zhang, S.-C. Chien, K.-S. Chen, H.-L. Yip, Y. Sun, J. A. Davies, F.-C. Chen, A. K. Y. Jen, *Chem. Commun.* **2011**, *47*, 11026.

[42] F. C. Krebs, H. Spanggaard, *Sol. Energy Mater. Sol. Cells* **2005**, *88*, 363.

[43] X. Zhang, M. Köhler, A. J. Matzger, *Macromolecules* **2004**, *37*, 6306.

© 2013 WILEY-VCH Verlag GmbH & Co. KGaA, Weinheim